Over-the-Air Testing of 5G Communication Systems: Validation of the Test Environment in Simple-Sectored Multiprobe Anechoic Chamber Setups

Fan, Wei; Zhang, Fengchun; Wang, Zhengpeng

Published in:
I E E E Antennas and Propagation Magazine

DOI (link to publication from Publisher):
10.1109/MAP.2019.2943305

Publication date:
2021

Document Version
Accepted author manuscript, peer reviewed version

Wei Fan, Fengchun Zhang, and Zhengpeng Wang

Over-the-Air Testing of 5G Communication Systems

Validation of the test environment in simple-sectored multiprobe anechoic chamber setups.

Over-the-air (OTA) radiated testing is seen as inevitable for 5G antenna systems. The simple-sectored multiprobe anechoic chamber (SS-MPAC) setup is a potential testing candidate for the evaluation of 5G antenna systems under real-world propagation conditions. Validation of emulated channel models in the practical SS-MPAC setup is essential, since it is important to ensure that the target channel models are correctly emulated. Our objective is to detect the joint-angle delay power profile of the reproduced channels in the SS-MPAC setup. In this article, we discuss two joint-angle delay estimation (JADE) algorithms: 1) an existing algorithm with high computation complexity as the reference method and 2) a novel, low-cost, sequential, 1D algorithm. Both numerical simulations and experimental verification measurements in a preliminary SS-MPAC setup are provided to validate the two discussed algorithms. The proposed sequential 1D search method is demonstrated to be highly accurate and effective and, therefore, is recommended for validation measurements in SS-MPAC setups. Measurement setup and procedures for test-environment validation are considered as well.

Digital Object Identifier 10.1109/MAP.2019.2943305
Date of current version: 15 October 2019

SS-MPAC SETUP

The demand for ubiquitous, reliable, and high-speed wireless connectivity has been steadily growing. Both massive multiple-input, multiple-output (MIMO) technology and the use of frequencies in the millimeter-wave (mm-wave) range are considered essential to addressing these challenges in the upcoming 5G systems. Radiated OTA testing [i.e., testing without the device under test (DUT) physically connected to the test equipment] has been seen as inevitable for 5G antenna systems [1]–[6]. The 5G antenna systems will be large scale, beam steerable, highly compact, and integrated. It is expected that antennas will be integrated into radio-frequency (RF) transceiver circuits, that is, with no place to probe or put connections. As a result, it will be impractical to use traditional RF connectors between the radio circuit and the antenna due to the integrated design, creating the need for OTA radiated testing.

It is important to test DUT performance in real-world propagation scenarios in the laboratory, where the DUT's end-to-end performance (including both radio and baseband parts) can be thoroughly evaluated [7], [8]. The MPAC method has been adopted in the standards for OTA performance testing of 4G LTE terminals due to its ability to test off-the-shelf DUTs, for which all critical parts of the design are evaluated at once [9]–[11]. The MPAC method offers a realistic test condition in which the device can operate normally with the help of a radio channel

emulator (CE). For LTE terminal testing, an MPAC setup with a 2D uniform OTA antenna configuration is typically adopted. A cost-effective 3D SS-MPAC configuration, as illustrated in Figure 1, has been examined for 5G antenna systems, including both the large-scale, sub-6-GHz, massive MIMO and mm-wave systems [2], [7], [12], [13].

By exploring the sparsity of radio channels and directivity of 5G antenna systems, the SS-MPAC setup can potentially reproduce target 3D channel models with reduced system cost. A fully flexible switching circuitry might not be practical due to design and cost challenges. Efforts should be taken to reduce switching-circuitry complexity while maintaining OTA system performance. The radiated two-stage (RTS) and reverberation-chamber (RC) methods are also reviewed for OTA testing of multiantenna systems [14]–[17]. However, the RTS method is not suitable for adaptive antenna systems, and the RC method is limited to 3D isotropic angular distributions. Standardization work toward OTA testing of 5G terminals is underway in 3rd Generation Partnership Project (3GPP) meetings. The MPAC solution has been selected as the reference method for sub-6-GHz 5G terminals, while the RTS method can be utilized after harmonization of test results with the MPAC method. The 3D MPAC solution has been selected for mm-wave 5G terminals as well.

In [13], the complete framework for the SS-MPAC setup is presented, including channel-emulation methods for mapping channel models onto probe antennas and setup design parameters (i.e., the measurement range, number and location of available probe antennas, number and location of active probe antennas, required radio CE resources, and so on). In [7], an overview of radiated testing methodologies for multiple-antenna systems and their applicability for adaptive mm-wave antenna systems are given, and the feasibility of each test-system component and the performance-evaluation metrics of the SS-MPAC method are explained. In [2] and [12], the applicability of the SS-MPAC method for mm-wave is discussed. In [18], a flexible CE design framework is proposed; the proposed CE structure is capable of frequency setting from the sub-6-GHz to mm-wave bands and flexible system-bandwidth setting. As pointed out in [13], calibration of the practical SS-MPAC systems and validation of emulated channel models in the practical SS-MPAC setup are essential and currently missing in the literature. Channel-model-validation measurements for conventional 2D MPAC have been widely reported in academia and industry (see, for example, [10], [11], and [19]–[21]) and standardized in the wireless communication industry in the United States Cellular Telecommunications Industry Association and the 3GPP.

The objective of the channel-validation measurement is to ensure that target channel models are correctly implemented inside the test area. Several aspects of the emulated channel models are analyzed in the channel-validation measurements, such as the fading distribution, power delay profile, power Doppler spectrum/temporal autocorrelation function, spatial correlation, and cross-polarization ratio [10], [11]. The spatial correlation, which is a statistical measure of the similarity between received signals at different spatial locations, has been used to represent the channel spatial characteristics at the receiver side and is selected as the figure of merit (FoM) for OTA testing in conventional MPAC setups. The spatial correlation is also popularly adopted in industry as the FoM due to the importance of correlation in LTE spatial-multiplexing testing. As explained in [7] and [13], the spatial correlation might be less relevant to determining OTA system performance for beam-steerable devices; the power angular spectra of the emulated channels are more interesting. Unlike 4G systems with limited bandwidths, 5G systems will offer a much larger frequency bandwidth, which implies a high delay resolution in the emulated channels.

The joint-angle delay power profile of the emulated channels is of interest in the channel-validation measurements in SS-MPAC setups. For this article, channel-validation measurements were performed in a preliminary SS-MPAC setup in an anechoic chamber, and two algorithms for obtaining the joint angle delay power profile of the emulated channels are debated. The main contributions of the article are the following.

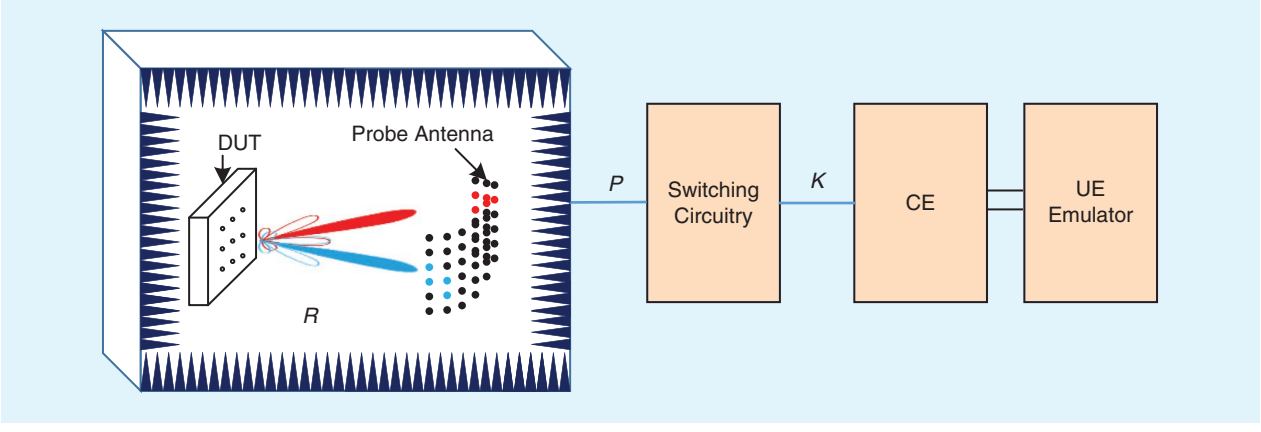

FIGURE 1. A schematic of the SS-MPAC setup implemented with switching circuitry. The available probe antennas (*P*) and active antennas (*K*) are indicated with black and red/blue dots, respectively. *P* and *K* denote the number of connections in the diagram. UE: user equipment.

- Two algorithms are considered for the joint-angle delay power profile of the emulated channels in the SS-MPAC setup: a high-computational JADE algorithm [22] and a new, low-cost, sequential, 1D search method.
- A channel-validation-measurement campaign is performed in a preliminary SS-MPAC setup, where the two discussed algorithms are applied and validated.
- A measurement procedure for channel-validation measurements that is suitable for the SS-MPAC setup is presented.

SIGNAL MODEL AND ESTIMATION METHODS

SIGNAL MODEL

Figure 2 illustrates an SS-MPAC setup, where a uniform circular array (UCA) is utilized in the test area to sample the emulated propagation channels. The number of probe antennas is K, and the number of UCA elements is M. The radius of the probe sphere, R, is assumed to be much larger than the radius of the UCA, r. A virtual uniform linear array (ULA) is typically adopted for the conventional MPAC setup due to its simplicity [10], [11]. However, ULAs are not able to distinguish propagation paths symmetric to the array axis and present nonconstant beam patterns over different scan angles. Unlike the ULA, the UCA has gained popularity since it presents approximately constant beam patterns over 360° azimuth angles, regardless of the scanning angle. A benefit of the UCA measurement system is that it requires only radial movement, which is achievable with existing positioner systems; that is, no extra measurement facility is needed. In principle, these two algorithms can be applied for arbitrary array configuration. The 3D array configuration (e.g., cylinder or cubic array) might present better performance due to its large antenna aperture compared to the UCA; however, it is not addressed in this article due to the requirements of long measurement time and extra positioning facilities.

The channel frequency responses (CFRs) at the M UCA elements at the nth channel snapshot $\boldsymbol{H}^n \in \mathbb{C}^{M\times L}$ (where L is the number of frequency points) can be written in a matrix form as

$$\boldsymbol{H}^n = [\boldsymbol{h}^n(f_1), \cdots, \boldsymbol{h}^n(f_L)], \tag{1}$$

where $\boldsymbol{h}^n(f_l) = \boldsymbol{A}(f_l)\cdot \boldsymbol{s}^n(f_l) \in \mathbb{C}^{M\times 1}$, with $\boldsymbol{s}^n(f_l) = \{s_k^n(f_l)\}_{K\times 1}$ and $\boldsymbol{A}(f_l) = \{a_{m,k}(f_l)\}_{M\times K}$. In this article, the notation $\boldsymbol{H} \in \mathbb{C}^{M\times L}$ denotes an $\boldsymbol{H}$ matrix with complex-valued elements and matrix size $M \times L$. The CFR at frequency point f_l and at the nth channel snapshot at the UCA center $s_k^n(f_l)$ can be expressed as

$$s_k^n(f_l) = \sum_{i=1}^{p_k} \alpha_{k,i} \exp(-j2\pi f_l \tau_{k,i}), \tag{2}$$

where $\alpha_{k,i}$ and $\tau_{k,i}$ denote the complex amplitude and delay of the ith path in the kth direction, respectively, and p_k denotes the total number of paths in the kth direction. The number of delay taps from one probe direction might be more than one in practical SS-MPAC setups for some applications. This is due to the fact that, in practical setups, the number of probe antennas is limited by cost considerations. As a result, one probe antenna might be utilized to synthesize several paths that have different delay profiles.

Under the plane wave assumption, $a_{m,k}(f_l)$ can be written as

$$a_{m,k}(f_l) = \exp\left[j\frac{2\pi f_l r \sin(\theta_k)\cos(\phi_k - \varphi_m)}{c}\right], \tag{3}$$

where θ_k and ϕ_k denote the elevation and azimuth angles of the kth probe antenna, respectively, as shown in Figure 2. $\varphi_m = 2\pi(m-1)/M$ for $m \in [1, M]$ denotes the angular location of the mth UCA element, and c is the speed of light. The goal is to estimate the joint-angle delay power profile of the emulated channels in the channel-validation measurements. That is, the objective is to estimate the channel parameters $\{\alpha_{k,i}, \tau_{k,i}, \theta_k, \phi_k\}$ based on the CFRs recorded by the virtual UCA. In the following sections, two algorithms are discussed for this purpose.

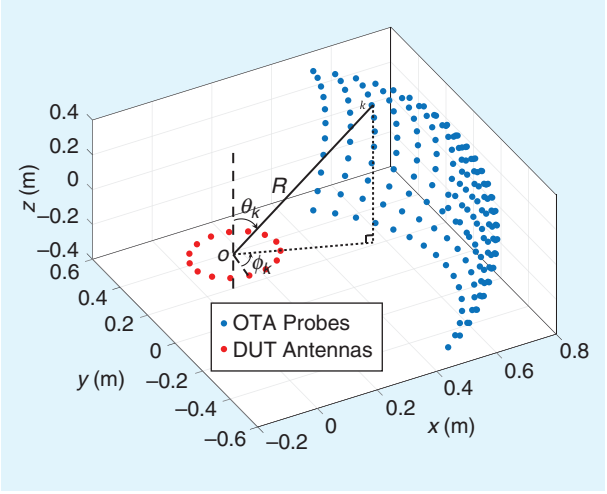

FIGURE 2. An illustration of the SS-MPAC setup and UCA in the test area.

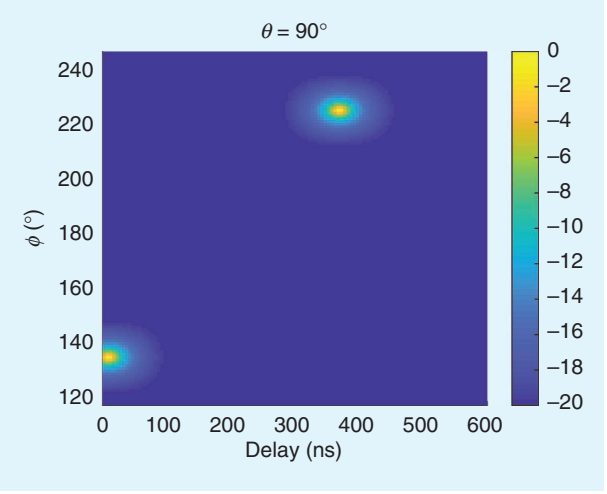

FIGURE 3. The joint-angle delay power profile at $\theta = 90°$ using the JADE algorithm.

JADE METHOD

From $\boldsymbol{H}^n$, we can construct a Hankel matrix $\underline{\boldsymbol{H}}^n \in \mathbb{C}^{ML' \times (L-L'+1)}$ by left-shifting and stacking L' copies of $\boldsymbol{H}^n$, which yields [22]

$$\underline{\boldsymbol{H}}^n = \begin{bmatrix} \boldsymbol{h}^n(f_1) & \boldsymbol{h}^n(f_2) & \cdots & \boldsymbol{h}^n(f_{L-L'+1}) \\ \boldsymbol{h}^n(f_2) & \boldsymbol{h}^n(f_3) & \cdots & \boldsymbol{h}^n(f_{L-L'+2}) \\ \vdots & \vdots & \cdots & \vdots \\ \boldsymbol{h}^n(f_{L'}) & \boldsymbol{h}^n(f_{L'+1}) & \cdots & \boldsymbol{h}^n(f_L) \end{bmatrix}. \tag{4}$$

The covariance matrix of $\underline{\boldsymbol{H}}^n$ can be expressed as

$$\underline{\boldsymbol{R}} = \frac{1}{N}\sum_{n=1}^{N} \underline{\boldsymbol{H}}^n (\underline{\boldsymbol{H}}^n)^H \in \mathbb{C}^{ML' \times ML'}, \tag{5}$$

where $()^H$ denotes the Hermitian transpose operation.

We can then apply the multiple signal classification (MUSIC) algorithm to obtain the angle delay estimates. MUSIC is a subspace-based algorithm that offers high angle- and delay-estimation resolution. The basic idea is that we can search the steering vectors and find those that are orthogonal to the noise subspace. The pseudo-power spectrum is given by [23]

$$\underline{p}(\theta,\phi,\tau) = \frac{1}{\underline{\boldsymbol{w}}(\theta,\phi,\tau)\,\underline{\boldsymbol{\nu}}\underline{\boldsymbol{\nu}}^H \underline{\boldsymbol{w}}^H(\theta,\phi,\tau)}, \tag{6}$$

where $\underline{\boldsymbol{\nu}}$ is the noise subspace eigenvectors obtained from the eigenmode decomposition of covariance matrix $\underline{\boldsymbol{R}}$. Define $\boldsymbol{v}(\theta,\phi,\tau) = \{v_{m,l'}(\theta,\phi,\tau)\}_{M\times L'}$ with

$$v_{m,l'}(\theta,\phi,\tau) = \exp\left[-j\frac{2\pi f_{l'} r \sin(\theta)\cos(\phi-\varphi_m)}{c} + j2\pi f_{l'}\tau\right]. \tag{7}$$

The steering vector $\underline{\boldsymbol{w}}(\theta,\phi,\tau) \in \mathbb{C}^{1\times ML'}$ can be formed as

$$\underline{\boldsymbol{w}}(\theta,\phi,\tau) = \{\mathrm{vec}[\boldsymbol{\nu}(\theta,\phi,\tau)]\}^T, \tag{8}$$

where vec() and $()^T$ denote the vectorization and matrix transpose operations, respectively.

From (6), we can obtain the angle and delay estimates $(\hat{\theta}_k, \hat{\phi}_k, \hat{\tau}_{k,i})$ for $k \in [1,K]$ and $i \in [1,p_k]$ directly via searching the elevation angle, azimuth angle, and delay space. As explained, (6) checks only the orthogonality between the steering vectors and noise spaces, and, hence, power estimates are inconsistent with the true power. Next, we explain how to retrieve the consistent power estimate based on the angle and delay estimates obtained in (6).

The CFR of the UCA array at the nth channel snapshot $\underline{\boldsymbol{Y}}^n \in \mathbb{C}^{1\times L}$ can be written as

$$\underline{\boldsymbol{Y}}^n = \boldsymbol{w}(\hat{\theta}_k, \hat{\phi}_k)\cdot \boldsymbol{H}^n, \tag{9}$$

where $\boldsymbol{\omega}(\hat{\theta}_k, \hat{\phi}_k) = \{\omega_m(\hat{\theta}_k, \hat{\phi}_k)\}_{1\times M}$ is the complex weight vector of the UCA for the kth path direction. First, we need to steer the beam pattern to the estimate angle $(\hat{\theta}_k, \hat{\phi}_k)$, that is, with the complex weight vector set to

$$\omega_m(\hat{\theta}_k, \hat{\phi}_k) = \exp\left[-j\frac{2\pi f_c r \sin(\hat{\theta}_k)\cos(\hat{\phi}_k - \varphi_m)}{c}\right], \tag{10}$$

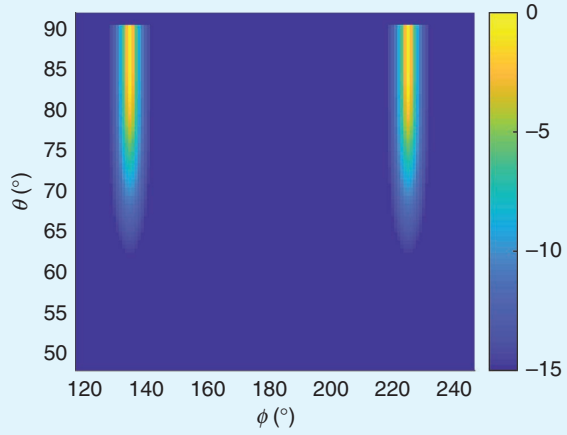

FIGURE 4. The power angle spectrum for the sequential search algorithm.

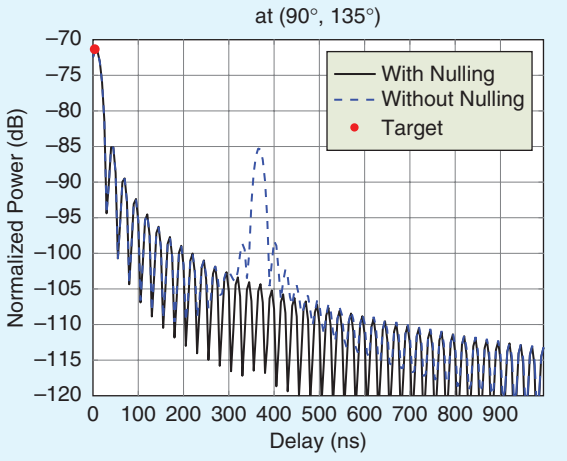

FIGURE 5. The UCA CIR with angle steering to $\hat{\theta} = 90^\circ$ and $\hat{\phi} = 135^\circ$.

where f_c is the carrier frequency. Performing an inverse Fourier transform of the array frequency response $\underline{\boldsymbol{Y}}^n$, we can obtain the array channel-impulse response (CIR) $\underline{\boldsymbol{y}}^n \in \mathbb{C}^{1\times L}$. Therefore, the sum power over N snapshots $\underline{\boldsymbol{p}} \in \mathbb{R}^{1\times L}$ can be calculated as

$$\underline{\boldsymbol{p}}(\hat{\theta}_k, \hat{\phi}_k) = \sum_{n=1}^{N} \underline{\boldsymbol{y}}^n \odot (\underline{\boldsymbol{y}}^n)^*, \tag{11}$$

where $\odot$ and $()^*$ denote element-wise multiplication and complex conjugate operations, respectively. The power estimate at $(\hat{\theta}_k, \hat{\phi}_k, \hat{\tau}_{k,i})$ can be obtained via setting $\tau = \tau_{k,i}$ in $\underline{\boldsymbol{p}}(\hat{\theta}_k, \hat{\phi}_k)$ directly as

$$\hat{\underline{p}}(\hat{\theta}_k, \hat{\phi}_k, \hat{\tau}_{k,i}) = \underline{\boldsymbol{p}}(\hat{\theta}_k, \hat{\phi}_k)\big|_{\tau=\tau_{k,i}}. \tag{12}$$

The selection of L' in (4) is a tradeoff between delay resolution and computation complexity. As shown in (4), a subband

can be selected by setting L'. A small L' offers low computation complexity, and the delay resolution is reduced as well due to small selected subband bandwidth. Taking $L' = 1$ as an extreme case, we will obtain only the angle estimates with low computation complexity, while the delay estimates will not be available due to a single selected frequency point. The algorithm complexity will scale up significantly due to the large matrix dimension of the correlation matrix $\underline{\boldsymbol{R}}$ in (5) and 3D brute-force search in the elevation angle, azimuth angle, and delay domain in (6).

SEQUENTIAL 1D SEARCH METHOD

To reduce the computation complexity, a sequential 1D search method is presented. In the two-stage sequential search method, we first obtain angle estimates based on the MUSIC algorithm, and then the delay power spectra are obtained based on those angle estimates.

The covariance matrix of $\boldsymbol{H}^n$ can be calculated as

$$\boldsymbol{R} = \sum_{n=1}^{N}\sum_{l=1}^{L} \boldsymbol{h}^n(fl)(\boldsymbol{h}^n(fl))^H \in \mathbb{C}^{M\times M}. \tag{13}$$

Again, we can obtain the angle estimates by applying the MUSIC algorithm as

$$p(\theta,\phi) = \frac{1}{\boldsymbol{\omega}(\theta,\phi)\boldsymbol{\nu}\boldsymbol{\nu}^H\boldsymbol{\omega}^H(\theta,\phi)}, \tag{14}$$

where $\boldsymbol{\omega}(\theta,\phi)$ is the steering vector of the UCA as discussed earlier, and $\boldsymbol{\nu}$ are eigenvectors obtained from eigenmode decomposition of $\boldsymbol{R}$ spanned to the noise space. The angle estimates $(\hat{\theta}_k,\hat{\phi}_k)$ for $k \in [1,K]$ can be obtained by finding the peaks of the power spectra in (14).

After obtaining $(\hat{\theta}_k,\hat{\phi}_k)$ for $k \in [1,K]$, the next step is to estimate delays for each estimated angle direction. To ensure that the delay estimates at the target direction are not affected by paths from other interfering directions, we can form the beam to the target signal direction [i.e., $(\hat{\theta}_k,\hat{\phi}_k)$] and the nulls to the other $K-1$ interfering signal directions [i.e., $(\hat{\theta}_i,\hat{\phi}_i)$ for $i \in [1,K-1]$ and $i \neq k$]. This operation of UCA is computationally cheap, since it requires only beamforming and nulling operations over the spatial domain. The complex weight vector $\boldsymbol{\Lambda}(\hat{\theta}_k,\hat{\phi}_k) \in \mathbb{C}^{1\times M}$ can be written as [23]

$$\boldsymbol{\Lambda}(\hat{\theta}_k,\hat{\phi}_k) = \boldsymbol{\omega}(\hat{\theta}_k,\hat{\phi}_k)[I_M - \boldsymbol{\Omega}(\boldsymbol{\Omega}^H\boldsymbol{\Omega})^{-1}\boldsymbol{\Omega}^H], \tag{15}$$

where $\boldsymbol{\omega}(\hat{\theta}_k,\hat{\phi}_k)$ is the UCA steering vector at $(\hat{\theta}_k,\hat{\phi}_k)$ in (7), $\boldsymbol{I}_M$ is a unit matrix of size M, and $\boldsymbol{\Omega}$ is the nulling matrix $\boldsymbol{\Omega} = \{\Omega_{m,i}\} \in \mathbb{C}^{M\times(K-1)}$ with

TABLE 1. THE PATH PARAMETERS FOR THE SIMULATION.

Path Index	Power (dB)	Delay (ns)	Angle
1	0	0	$\theta_1 = 90^\circ, \phi_1 = 135^\circ$
2	–2	365	$\theta_2 = 90^\circ, \phi_2 = 225^\circ$

$$\Omega_{m,i} = \exp\left[-j\frac{2\pi f_c r\sin(\hat{\theta}_i)\cos(\hat{\phi}_i - \varphi_m)}{c}\right]. \tag{16}$$

Similarly, we can obtain the CFR of the UCA array as

$$\boldsymbol{Y}^n = \boldsymbol{\Lambda}(\hat{\theta}_k,\hat{\phi}_k)\cdot\boldsymbol{H}^n. \tag{17}$$

Therefore, the power delay profile at the kth direction can be calculated as

$$\boldsymbol{p}(\hat{\theta}_k,\hat{\phi}_k,\tau) = \sum_{n=1}^{N}\boldsymbol{y}^n \odot (\boldsymbol{y}^n)^*. \tag{18}$$

The power and delay estimates for $i \in [1,p_k]$ can be then obtained from the peaks for the power delay profile. Compared to the JADE algorithm, the two-stage sequential method can significantly reduce the computation complexity due to the reduced size of $\boldsymbol{R}$ in (13) compared to $\underline{\boldsymbol{R}}$ in (5) and the 2D (i.e., elevation and azimuth angles) search in (14) compared to the 3D search in (6).

SIMULATION RESULTS

In this section, the two algorithms are numerically validated. A UCA composed of 15 isotropic elements with $r = 0.14$ m is utilized. The frequency is set to 2.45 GHz with a bandwidth of 40 MHz. R is set to 2 m. The simulation parameters are set according to the measurement setups, which will be discussed later. Two paths are emulated for simplicity, as detailed in Table 1. The two emulated paths are time-variant fading channels generated with the geometry-based stochastic channel (GBSC) principles with cluster (path) parameters defined in Table 1.

JADE

The joint-angle delay power profile can be calculated from (6). The power spectrum peaks at $\theta = 90^\circ$, meaning that the elevation angle estimate is $\hat{\theta} = 90^\circ$. The angle delay power profile using the JADE algorithm at $\hat{\theta}_1 = \hat{\theta}_2 = 90^\circ$ is shown in Figure 3. From the peaks in the power spectrum, we can obtain the azimuth angle and delay estimates of the emulated paths directly. The angle and delay estimates match well with the targets, as shown in Figure 3. With $(\hat{\theta}_k,\hat{\phi}_k,\hat{\tau}_k)$ for $k \in [1,2]$, we can obtain the power estimate $\hat{p}_k$ directly in (12). The power estimates agree with the target values. Therefore, the JADE algorithm can accurately estimate the joint-angle delay power profile. However, as explained, its main drawback is its high computation complexity. The elevation-angle resolution is constrained by the limited capabilities of UCA for angle detection in the elevation plane.

SEQUENTIAL SEARCH ALGORITHM

To use the sequential search algorithm, we first need to obtain the angle estimates. Applying the MUSIC algorithm in (14), we can obtain pseudo-power spectra, as shown in Figure 4, where two paths can be identified. The angle estimates of the two paths match well with the target values (i.e., $\hat{\theta}_1 = 90^\circ$, $\hat{\phi}_1 = 135^\circ$ and $\hat{\theta}_2 = 90^\circ$, $\hat{\phi}_2 = 225^\circ$). As previously discussed, the elevation-angle resolution of the UCA is limited. Steering the UCA beam toward path one at $\hat{\theta} = 90^\circ$ and $\hat{\phi} = 135^\circ$, we

can obtain the UCA power delay profile, as shown in Figure 5. Consequently, we form the beam to the target signal direction and the nulls to the other interfering signal directions at the same time to ensure that the delay estimates at the target direction are not affected by paths from other interfering directions. Figure 5 shows that, without performing the nulling operation (i.e., steering the beam only to the target angle direction), we might conclude that two paths (one with delay 0 ns and the other with delay 365 ns) exist at direction $\hat{\theta} = 90^\circ$, $\hat{\phi} = 135^\circ$. Steering the UCA beam toward path two at $\hat{\theta} = 90^\circ$ and $\hat{\phi} = 225^\circ$, we can obtain the UCA power delay profile shown in Figure 6. Similarly, it can be observed that the nulling operation is necessary to obtain the true delay estimates in the target directions. Although good estimation accuracy is achieved with both the existing JADE and sequential search algorithms, the proposed sequential search method offers significantly lower computation complexity.

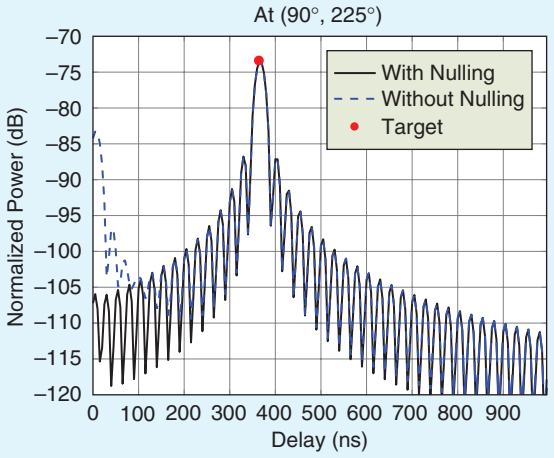

FIGURE 6. The UCA CIR with angle steering to $\hat{\theta} = 90^\circ$ and $\hat{\phi} = 225^\circ$.

MEASUREMENT VALIDATIONS

MEASUREMENT SETUP

An illustration of the multiprobe measurement setup is shown in Figure 7; it consists of a vector network analyzer (VNA), a Propsim radio CE, three dual-polarized horn antennas as OTA antennas, and a vertically polarized sleeve dipole. Only three vertically polarized ports of the OTA antennas were connected to the CE output interface ports for simplicity. Although the channel-validation measurements were done in a preliminary SS-MPAC, the considered algorithms can be applied to arbitrary MPAC setups and channel models in principle.

As shown in Figure 7, time-variant CIRs can be loaded and implemented in the CE and radiated by the OTA probe antennas. Typically, the CIRs can be generated based on the GBSC [24]–[27] or correlation-based channel-modeling principles [28]. In our measurement, three time-variant CIRs loaded in the CE are generated by following the GBSC principle, giving $h_k(t,\tau) \in \mathbb{C}^{10000\times 18}$ for $k \in [1,K]$ with 10,000 time snapshots and 18 delay taps, respectively. A photo of the practical setup is shown in Figure 8. A vertically oriented sleeve dipole at 2,450 MHz is rotated 15 times with a 24° step to form a UCA. The distance of the sleeve dipole to the virtual UCA center is

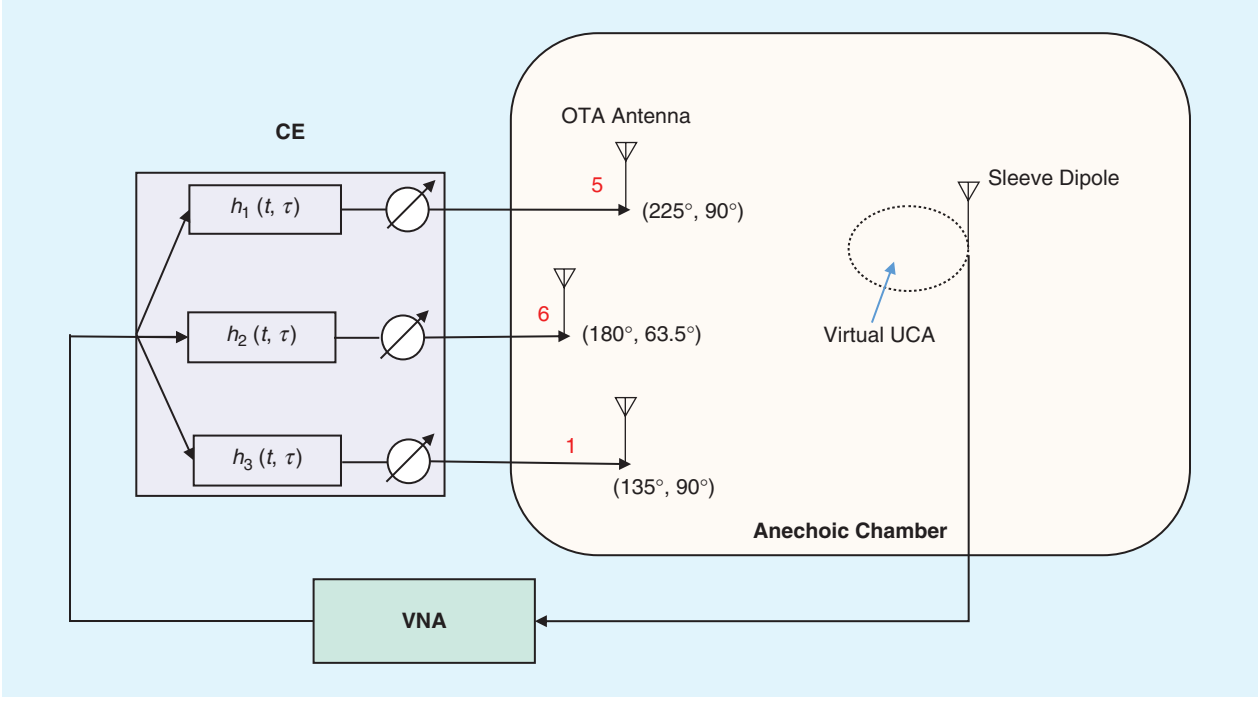

FIGURE 7. An illustration of the SS-MPAC validation setup. The angular locations and indexes of the OTA antennas are shown.

0.14 m (i.e., the UCA radius is 0.14 m). With the help of the CE, the emulated channels are repeatable and controllable in the anechoic chamber. Therefore, we have the ability to run the emulation to a specific time snapshot of the CIR, pause the emulation there, and measure its CFR with the VNA. Similar to the spatial-correlation measurement procedure specified in the standards [10], we record the CFR in the VNA every 10 CIRs to ensure independent CIR realizations. The virtual UCA can be formed, since we can replay the same CIRs in the CE for every position of the UCA in a controllable manner. Therefore, for each measurement location, we record a total of 1,001 CFRs. In the VNA, the center frequency is set to 2.45 GHz, with 40-MHz bandwidth and 1,601 frequency samples. The frequency bandwidth is constrained by the limitation of the RF bandwidth in the CE [29]. The measured data dimension, as a result, is $15 \times 1,601 \times 1,001$ (i.e., number of measured locations × number of frequency samples × number of snapshots).

TARGET CHANNEL MODELS

For the sake of simplicity, the channel parameters in the standard spatial channel model extended (SCME) urban macro (UMa) tap delay line model is selected to generate three CIRs, $h_k(t,\tau) \in \mathbb{C}^{10000\times 18}$ for $k \in [1,K]$. An illustration of the time-variant CIRs radiated from a probe antenna is shown in Figure 9. As discussed in [24], the SCME UMa channel model consists of six paths, and each path is composed of three midpaths with a delay separation of 5 ns between them. The six fading paths with different delay and power levels can be clearly observed. Following the GBSC principle, the three fading CIRs are independent and identically distributed. The spatial profile of the SCME UMa model is not implemented. Only the fading profiles are realized in the CE. For 4G LTE terminal OTA testing, the target channel models are the SCME channel models. For the 5G case, the 3GPP 38.901 channel models are actively discussed in the standards for performance testing. However, in the article, the target test environment is simplified, as defined in Figure 10. In principle, the discussed measurement procedure and algorithms work for any SS-MPAC setups and spatial-channel models.

As explained, for MIMO OTA testing of LTE terminals, the power delay profile and spatial correlation were separately

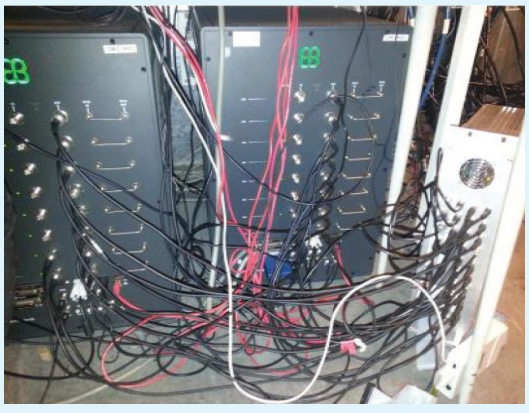

(a)

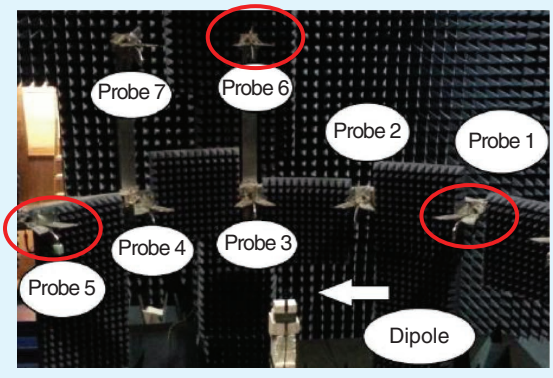

(b)

FIGURE 8. The measurement setup: (a) the Propsim CE and (b) the sectored MPAC configuration. The active OTA antennas are marked in red.

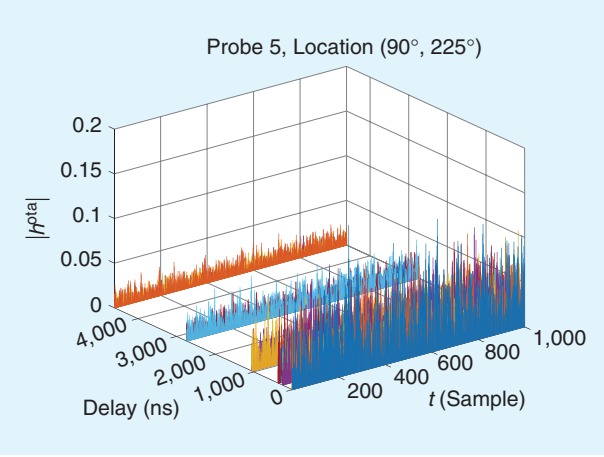

FIGURE 9. An illustration of the radiated CIRs from probe 1.

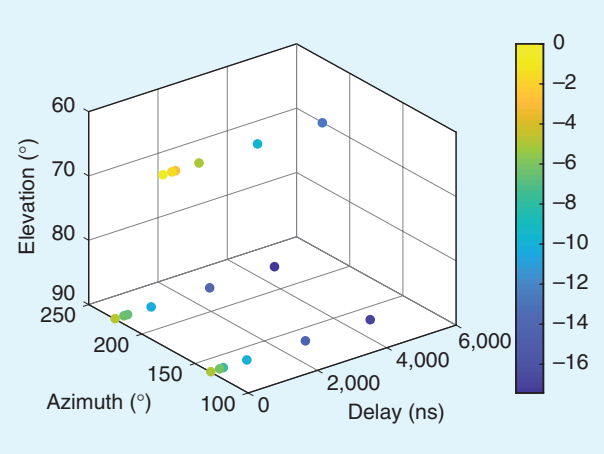

FIGURE 10. The target power angle delay profile in the measurement.

measured in the channel-validation measurements [10], [11], [19]. For the power-delay-profile validation measurement, the CIRs are recorded only at one position, that is, the center of the test zone. For the spatial correlation measurements, the CIRs are recorded at multiple positions, with center frequency and zero span set in the VNA. In this article, the target is the joint-angle delay power profile validation. Therefore, we need to record the CIRs over supported bandwidth for all UCA element positions, indicating a long measurement time. The measurement time took approximately 10 h in our research.

The angular positions of the OTA antennas are shown in Figure 7. Therefore, the target angle delay power profile of the emulated channels observed in the test zone can be visualized in Figure 10. The main objective of the validation measurements is to check whether all parameters of the angle delay power profile can be accurately detected. From each probe direction, we have six paths generated in the delay domain in the CE. The target channel model is generated on purpose to evaluate the robustness of the algorithm, although it might not be realistic in practice.

RESULTS AND DISCUSSION

JADE METHOD

Applying the JADE method, we can obtain the joint-angle delay profile directly. The power spectra peak around $\theta = 79^\circ$ and $\theta = 60^\circ$, which differs slightly from the targets of $\theta = 90^\circ$ and $\theta = 63.5^\circ$, respectively. The joint-angle delay profiles at $\theta = 90^\circ$ and $\theta = 79^\circ$ are shown in Figures 11 and 12, respectively. The peak power at $\theta = 90^\circ$ is approximately 2 dB less than that at $\theta = 79^\circ$. The elevation angle estimation deviation might be caused by several issues. The UCA aperture is small in

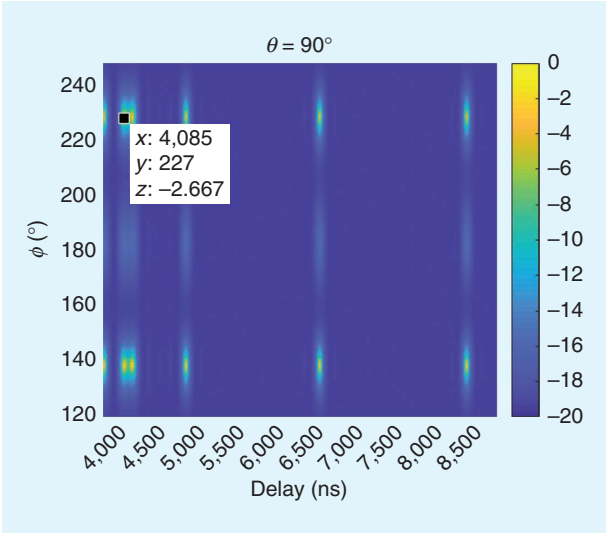

FIGURE 11. The measured joint-angle delay power profile at $\theta = 90^\circ$ using the JADE algorithm.

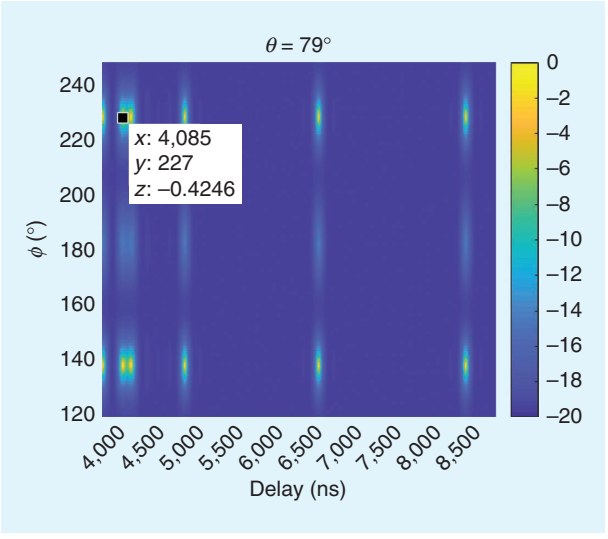

FIGURE 12. The measured joint-angle delay power profile at $\theta = 79^\circ$ using the JADE algorithm.

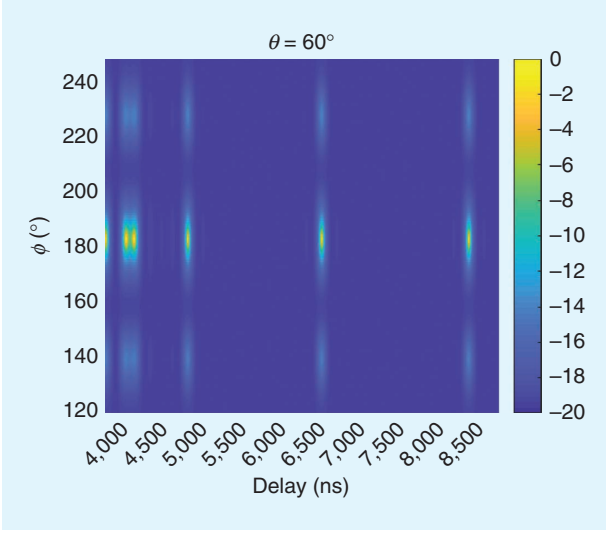

FIGURE 13. The measured joint-angle delay power profile at $\theta = 60^\circ$ using the JADE algorithm.

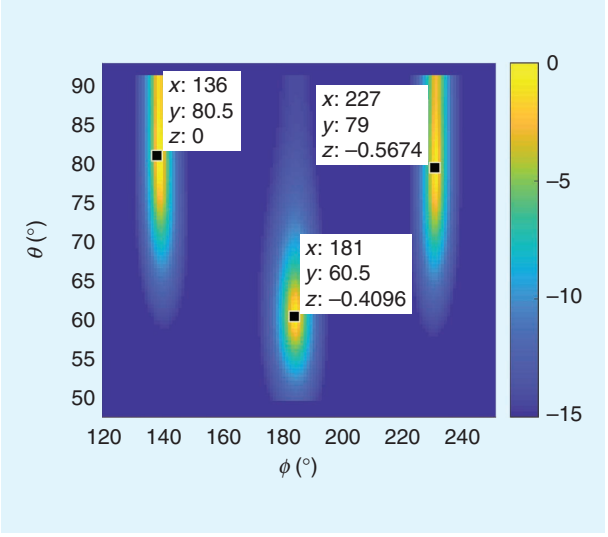

FIGURE 14. The measured power angle spectrum for the sequential search algorithm.

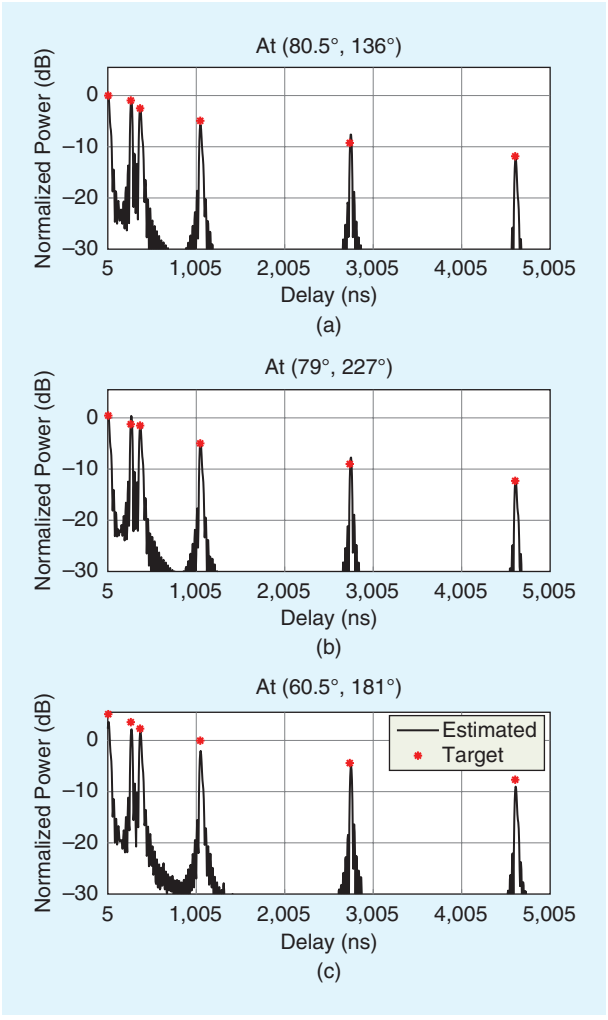

FIGURE 15. The measured UCA CIR with angle steering to (a) $(\hat{\theta}_1 = 80.5^\circ, \hat{\phi}_1 = 136^\circ)$, (b) $(\hat{\theta}_2 = 79^\circ, \hat{\phi}_2 = 227^\circ)$, and (c) $(\hat{\theta}_3 = 60.5^\circ, \hat{\phi}_3 = 181^\circ)$.

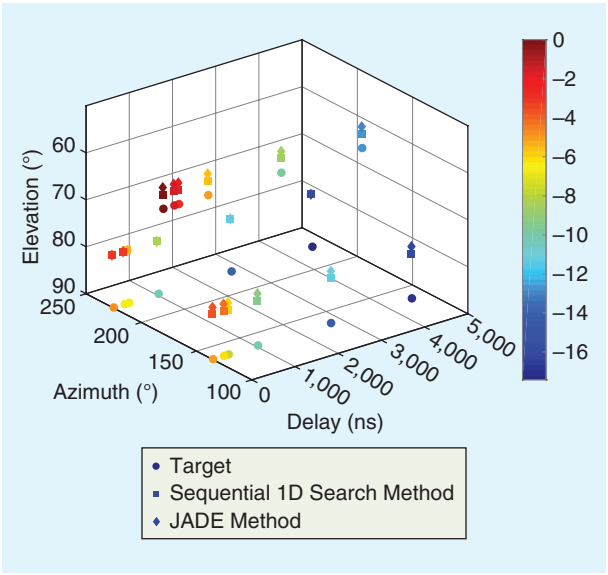

FIGURE 16. The target and measured angle delay power profiles.

elevation, leading to nonrobust elevation-angle estimation. The phase center of the sleeve dipole might differ from its specification in practical setup due to cable effects. Furthermore, the height of the sleeve dipole might not coincide with the OTA ring, leading to elevation-angle estimation errors. From the power profiles shown in Figures 12 and 13, we can see that the azimuth angle and delay estimates agree well with the target values.

SEQUENTIAL SEARCH ALGORITHM

The measured power angle spectrum for the sequential search method is shown in Figure 14, where three paths are identified, with estimated angles $(\hat{\theta}_1 = 80.5^\circ, \hat{\phi}_1 = 136^\circ)$, $(\hat{\theta}_2 = 79^\circ, \hat{\phi}_2 = 227^\circ)$, and $(\hat{\theta}_3 = 60.5^\circ, \hat{\phi}_3 = 181^\circ)$. The azimuth-angle estimates of the three path directions match well with the target values. However, similar to the reference JADE algorithm, some small deviation exists for the elevation-angle estimation. As shown in Figure 14, the elevation-angle resolution is rather small due to the small elevation antenna aperture of the UCA.

Steering the beams to the three detected directions, we can plot the power delay profiles of the UCA, as shown in Figure 15. The resulting power delay profiles are shifted in delay and power such that the first delay tap at direction $(\hat{\theta}_1 = 80.5^\circ, \hat{\phi}_1 = 136^\circ)$ is on delay 0 ns, and the peak power value is 0 dB. As shown in Figure 15, the delay estimates match well with the target for all three directions. The deviation in power up to 1.5 dB can be observed for all of the delay taps. The power estimates at direction $(\hat{\theta}_1 = 60.5^\circ, \hat{\phi}_1 = 181^\circ)$ are smaller than the target values due to the dipole-antenna radiation patterns. Paths that are not on the azimuth plane will be filtered by the dipole radiation patterns. The further the paths move away from the azimuth plane, the more power reduction of the paths we can expect.

The estimated angle delay power profiles using the two discussed algorithms and the target profiles are shown in Figure 16. As discussed, the azimuth, delay, and power estimates are accurate, but a small deviation exists for the elevation-angle estimates due to the small elevation aperture and system nonidealities in practical setups. As explained, we can improve the elevation angle estimation accuracy by utilizing 3D antenna arrays, which offer a large elevation antenna aperture. However, this also requires more measurement time and complicated mechanical movement.

CONCLUSIONS

The radiated OTA testing methodology is essential for performance evaluation of 5G antenna systems due to the integrated antenna and transceiver design. The SS-MPAC setup has the potential to reproduce realistic propagation conditions for 5G system-performance evaluation with reduced costs compared to conventional MPAC setups. Validation of emulated channels in the SS-MPAC setup is necessary to ensure that target test conditions are accurately mimicked in the anechoic chamber. For 5G applications, the joint-angle delay power profile is interesting for beamforming-management performance evaluations. In this article, two algorithms are discussed to estimate the joint-angle

power delay profiles of the emulated channels: a reference algorithm and a novel sequential search method. Both methods are numerically and experimentally validated. The channel-validation measurements in the preliminary SS-MPAC setup show that the power azimuth delay estimates are accurate for both methods, whereas a small deviation exists in the elevation-angle estimate due to the UCA's limited ability to estimate elevation angle. The proposed sequential method offers the same estimation accuracy but with significantly reduced computation complexity compared to the reference method. Hence, it is recommended for channel-validation measurements in SS-MPAC setups for 5G-system performance testing.

ACKNOWLEDGMENT

We appreciate the valuable comments from Yilin Ji with Aalborg University, Denmark, and Dr. Pekka Kyosti with Keysight Technologies, Oulu, Finland, and Oulu University.

AUTHOR INFORMATION

Wei Fan (wfa@es.aau.dk) is an associate professor in the Antenna, Propagation, and Millimeter-Wave Systems Section, Aalborg University, Denmark. His current research interests include over-the-air testing of multiple antenna systems, radio channel sounding, modeling, and emulation.

Fengchun Zhang (fz@es.aau.dk) is a research assistant with the Department of Electronics Systems, Aalborg University, Denmark. Her current research interests include antenna-array signal processing and radio channel characterization.

Zhengpeng Wang (wangzp@buaa.edu.cn) is an associate professor with Beihang University, Beijing, China. His current research interests include reconfigurable antennas, millimeter-wave antennas, feed antennas, and 5G over-the-air measurement.

REFERENCES

[1] Y. Qi et al., "5G over-the-air measurement challenges: Overview," *IEEE Trans. Electromagn. Compat.*, vol. 59, no. 6, pp. 1661–1670, Dec. 2017.
[2] Y. Jing, M. Rumney, H. Kong, and Z. Wen, "Overview of 5G UE OTA performance test challenges and methods," in *Proc. 2018 IEEE MTT-S International Wireless Symposium (IWS)*, May 2018, pp. 1–4.
[3] Keysight Technologies, "Testing 5G: Evolution or revolution?" Keysight Technol., New Delhi, India, Tech. Rep., Oct. 2016.
[4] Keysight Technologies, "Modelling what matters: Keeping a correct focus on 5G," Keysight Technol., New Delhi, India, Tech. Rep., Oct. 2016.
[5] M. Rumney, "Testing 5G: Time to throw away the cables," *Microw. J.*, vol. 59, no. 11, pp. 10–18, Nov. 2016.
[6] M. Gustafsson, T. Jämsä, and M. Högberg, "OTA methods for 5G BTS testing survey of potential approaches," in *Proc. XXXIInd General Assembly and Scientific Symp. Int. Union of Radio Science (URSI GASS)*, Aug. 2017, pp. 1–4.
[7] W. Fan, P. Kyosti, M. Rumney, X. Chen, and G. F. Pedersen, "Over-the-air radiated testing of millimeter-wave beam-steerable devices in a cost-effective measurement setup," *IEEE Commun. Mag.*, vol. 56, no. 7, pp. 64–71, July 2018.
[8] D. He, B. Ai, K. Guan, L. Wang, Z. Zhong, and T. Kürner, "The design and applications of high-performance ray-tracing simulation platform for 5G and beyond wireless communications: A tutorial," *IEEE Commun. Surveys Tuts.*, vol. 21, no. 1, pp. 10–27, Firstquarter 2019.
[9] P. Kyösti, T. Jämsä, and J.-P. Nuutinen, "Channel modelling for multiprobe over-the-air MIMO testing," *Int. J. Antennas Propag.*, vol. 2012, Mar. 2012, Art. no. 615954. doi: 10.1155/2012/615954.
[10] CTIA, "Test plan for 2 × 2 downlink MIMO and transmit diversity over-the-air performance," CTIA Certification, CTIA, Washington, D.C., Tech. Rep. Version 1.0, Aug. 2015.
[11] "Verification of radiated multi-antenna reception performance of User Equipment (UE)," 3rd Generation Partnership Project, Tech. Rep. 3GPP TR 37.977 V14.0.0, June 2016.
[12] A. Hekkala, P. Kysti, J. Kyrlinen, L. Hentil, and W. Fan, "Performance evaluation of sectored MPAC for 5G UE antenna systems," in *Proc. 6th Asia-Pacific Conf. Antennas and Propagation (APCAP)*, Oct. 2017, pp. 1–3.
[13] P. Kysti, L. Hentil, W. Fan, J. Lehtomki, and M. Latva-Aho, "On radiated performance evaluation of massive MIMO devices in multiprobe anechoic chamber OTA setups," *IEEE Trans. Antennas Propag.*, vol. 66, no. 10, pp. 5485–5497, Oct. 2018.
[14] X. Chen et al., "Reverberation chambers for over-the-air tests: An overview of two decades of research," *IEEE Access*, vol. 6, pp. 49,129–49,143, Aug. 2018.
[15] X. Chen, M. Zhang, S. Zhu, and A. Zhang, "Empirical study of angular–temporal spectra in a reverberation chamber," *IEEE Trans. Antennas Propag.*, vol. 66, no. 11, pp. 6452–6456, Nov. 2018.
[16] W. Yu, Y. Qi, K. Liu, Y. Xu, and J. Fan, "Radiated two-stage method for LTE MIMO user equipment performance evaluation," *IEEE Trans. Electromagn. Compat.*, vol. 56, no. 6, pp. 1691–1696, Dec. 2014.
[17] W. Fan, P. Kysti, L. Hentil, and G. F. Pedersen, "MIMO terminal performance evaluation with a novel wireless cable method," *IEEE Trans. Antennas Propag.*, vol. 65, no. 9, pp. 4803–4814, Sept. 2017.
[18] W. Fan, P. Kysti, L. Hentil, and G. F. Pedersen, "A flexible millimeter-wave radio channel emulator design with experimental validations," *IEEE Trans. Antennas Propag.*, vol. 66, no. 11, pp. 6446–6451, Nov. 2018.
[19] W. Fan, X. Carreno, J. S. Ashta, J. O. Nielsen, G. F. Pedersen, and M. B. Knudsen, "Channel verification results for the SCME models in a multi-probe based MIMO OTA setup," in *Proc. IEEE 78th Vehicular Technology Conf. (VTC Fall)*, Sept. 2013, pp. 1–5.
[20] L. Guo, C. Sun, X. An, X. Zhang, and M. Yang, "Over the air MIMO channel model validation," in *Proc. 7th European Conf. Antennas and Propagation (EuCAP)*, Apr. 2013, pp. 1848–1852.
[21] A. Scannavini, L. J. Foged, N. Gross, L. Hentila, J. Virtala, and K. Raju, "Test zone characterization for the multiprobe anechoic chamber setup (MPAC)," in *Proc. 10th European Conf. Antennas and Propagation (EuCAP)*, Apr. 2016, pp. 1–5.
[22] A.-J. Van Der Veen, M. C. Vanderveen, and A. J. Paulraj, "Joint angle and delay estimation using shift-invariance properties," *IEEE Signal Process. Lett.*, vol. 4, no. 5, pp. 142–145, May 1997.
[23] L. Harry and V. Trees, *Optimum Array Processing: Detection, Estimation, and Modulation Theory*. Hoboken, NJ: Wiley, 2002.
[24] D. S. Baum, J. Hansen, J. Salo, G. Del Galdo, M. Milojevic, and P. Kysti, "An interim channel model for beyond-3G systems: Extending the 3GPP spatial channel model (SCM)," in *Proc. IEEE 61st Veh. Technology Conf.*, vol. 5, Stockholm, Sweden: IEEE, May 2005, pp. 3132–3136.
[25] R. He, B. Ai, G. L. Stber, G. Wang, and Z. Zhong, "Geometrical-based modeling for millimeter-wave MIMO mobile-to-mobile channels," *IEEE Trans. Veh. Technol.*, vol. 67, no. 4, pp. 2848–2863, Apr. 2018.
[26] R. He, B. Ai, G. L. Stüber, and Z. Zhong, "Mobility model-based non-stationary mobile-to-mobile channel modeling," *IEEE Trans. Wireless Commun.*, vol. 17, no. 7, pp. 4388–4400, July 2018.
[27] X. Zhao, S. Li, Q. Wang, M. Wang, S. Sun, and W. Hong, "Channel measurements, modeling, simulation and validation at 32 GHz in outdoor microcells for 5G radio systems," *IEEE Access*, vol. 5, pp. 1062–1072, Jan. 2017.
[28] L. Schumacher and B. Dijkstra, "Description of a MATLAB implementation of the indoor MIMO WLAN channel model proposed by the IEEE 802.11 TGN channel model special committee," *Implementation Note Version*, vol. 5, pp. 1–27, Jan. 2004.
[29] Keysight Technologies, "Propsim F8 channel emulator," Keysight Technologies, New Delhi, India, Tech. Rep., Aug. 2016.